

Infrared Imaging of Magnetic Octupole Domains in Non-collinear Antiferromagnets

Peng Wang^{1,2,†}, Wei Xia^{3,4,†}, Jinhui Shen^{1,5}, Yulong Chen^{1,5}, Wenzhi Peng^{1,5},
Jiachen Zhang^{1,5}, Haolin Pan^{1,5}, Xuhao Yu^{1,5}, Zheng Liu^{5,6}, Yang Gao^{5,6},
Qian Niu^{5,6}, Zhian Xu³, Hongtao Yang⁷, Yanfeng Guo^{3,4,*}, and Dazhi Hou^{1,5,*}

¹*ICQD, School of Emerging Technology, University of Science and Technology of China, Hefei 230026, China*

²*College of Mathematics and Physics, Qingdao University of Science and Technology, Qingdao 266061, China*

³*School of Physical Science and Technology, ShanghaiTech University, Shanghai 201210, China*

⁴*ShanghaiTech Laboratory for Topological Physics, Shanghai 201210, China*

⁵*Department of Physics, University of Science and Technology of China, Hefei, Anhui 230026, China*

⁶*CAS Key Laboratory of Strongly-Coupled Quantum Matter Physics,*

University of Science and Technology of China, Hefei, Anhui 230026, China and

⁷*Xi'an Institute of Optics and Precision Mechanics of Chinese Academy of Sciences, Xi'an, Shanxi 710119, China*

Magnetic structure plays a pivotal role in the functionality of antiferromagnets (AFMs), which not only can be employed to encode digital data but also yields novel phenomena. Despite its growing significance, visualizing the antiferromagnetic domain structure remains a challenge, particularly for non-collinear AFMs. Currently, the observation of magnetic domains in non-collinear antiferromagnetic materials is feasible only in Mn_3Sn , underscoring the limitations of existing techniques that necessitate distinct methods for in-plane and out-of-plane magnetic domain imaging. In this study, we present a versatile method for imaging the antiferromagnetic domain structure in a series of non-collinear antiferromagnetic materials by utilizing the anomalous Etingshausen effect (AEE), which resolves both the magnetic octupole moments parallel and perpendicular to the sample surface. Temperature modulation due to the AEE originating from different magnetic domains is measured by the lock-in thermography, revealing distinct behaviors of octupole domains in different antiferromagnets. This work delivers an efficient technique for the visualization of magnetic domains in non-collinear AFMs, which enables comprehensive study of the magnetization process at the microscopic level and paves the way for potential advancements in applications.

Keywords: non-collinear antiferromagnets, domain structures, infrared imaging, anomalous Etingshausen effect

*Corresponding authors:

guoyf@shanghaitech.edu.cn;

dazhi@ustc.edu.cn.

[†]These two authors contributed equally to this work.

INTRODUCTION

The non-collinear antiferromagnet Mn_3X family has emerged as a significant class of materials in the field of spintronics[1–7]. These materials possess unique physical properties, including the magnetic spin Hall effect[8], the large anomalous Hall/Nernst effects (AHE/ANE)[9–11], the Weyl semimetal points[12], and the chiral domain wall memory effect[13]. Recent progress further demonstrated their electrical manipulation and readout capabilities, making them promising building elements for future memory devices[4, 5].

Therefore, the domain structure visualization in non-collinear antiferromagnet (AFM) is greatly pursued[14–22], which is indispensable for confirming and understanding the magnetic octupole dynamics driven by magnetic field and spin orbit torque[23–28]. Although the magneto-optical Kerr effect (MOKE) has been successfully used to image domain structures in Mn_3Sn [14, 16], it requires a pristine mirror surface and can image magnetic octupole domains with out-of-plane polarization with only few-nanometer depth[29]. The anomalous Nernst effect, on the other hand, can image octupole domain with in-plane polarization, but is limited to in-plane observations and is time-consuming for large devices due to the scanning approach[15]. Despite the early interests, the direct imaging and reconstruction of 3D rotation of octupole moments, which calls for simultaneous observation of both in-plane and out-of-plane octupole domains, remains elusive.

RESULTS AND DISCUSSION

Here, we demonstrate an alternative method for imaging the domain structure in non-collinear AFMs. We show that the domain structure can be imaged by the anomalous Ettingshausen effect (AEE) at room temperature, capturing octupole moments both parallel and perpendicular to the sample surface. The visualization of magnetic domains through the AEE was first demonstrated in ferromagnetic metals[30, 31]. The method is based on visualizing the spatial distribution of AEE-induced temperature modulations originating from different magnetic octupole domains, and is achieved through lock-in thermography (LIT)[32–34]. Employing the new technique, we achieve the observation of the octupole domain structure in Mn_3Sn and Mn_3Ge during both in-plane and out-of-plane magnetic reversals and reveal the out-of-plane rotation process of octupole moments in the memory effect of Mn_3Sn [13].

Figure 1a shows the magnetic structure of Mn_3Sn , which hosts a hexagonal crystal structure with $P6_3/mmc$ space group. Below its Néel temperature $T_N \approx 430$ K, it exhibits an inverse triangular spin structure of three neighboring Mn moments on its (0001)-plane kagome lat-

tice. This spin structure can be viewed as a ferroic order of a cluster magnetic octupole[35], which is comprised of six Mn atoms situated within two stacked kagome planes. The cluster magnetic octupole breaks the time-reversal symmetry macroscopically, which permits a non-zero net Berry curvature in momentum space[36, 37], thereby eliciting significant transverse responses, such as the large AHE and ANE[9–11, 38, 39]. Additionally, the competition between the Dzyaloshinskii-Moriya interaction and single-ion anisotropy results in a small net ferromagnetic moment through spin canting[40], which is essential for manipulating the direction of octupole moments using a magnetic field.

Magnetic domain imaging by the AEE

Figure 1b shows the set-up for infrared imaging of magnetic octupole domain structures using the AEE. In view of the large ANE in Mn_3Sn [10, 11], a large AEE in Mn_3Sn is expected by the Bridgman relation[41] between AEE and ANE. The AEE can convert a longitudinal electric current \mathbf{J}_c into a transverse heat current $\mathbf{J}_{q,AEE}$ that is dependent on the direction of the octupole moment in Mn_3Sn . The heat current generates a thermal gradient ∇T_{AEE} , so the phenomena of AEE can be described as

$$\nabla T_{AEE} = \varepsilon_{AEE}(\mathbf{j}_c \times \mathbf{p}), \quad (1)$$

where \mathbf{j}_c is the charge current density, \mathbf{p} is the unit vector of the octupole moment, ε_{AEE} is the anomalous Ettingshausen coefficient. Therefore, by measuring the AEE-induced temperature distribution on the sample surface, one can reveal the underlying octupole domain structures.

In particular, when an in-plane current is applied, the domains with opposite out-of-plane \mathbf{p} generate opposite in-plane thermal gradients on the sample surface (top view of Fig. 1b), while the domains with opposite in-plane \mathbf{p} produce either a cold or hot region on the sample surface (front view of Fig. 1b). To capture both scenarios with a much-improved temperature resolution (0.1 mK), LIT is utilized[32–34]. In this work, thermal images of the sample surface are captured while applying a rectangular-wave-modulated charge current with amplitude J_c , and frequency $f = 16.25$ Hz. The use of such current allows for the extraction of thermoelectric effects ($\propto J_c$) free from the Joule-heating background ($\propto J_c^2$)[42, 43]. Fourier analyses are performed to extract the first harmonic response of the detected thermal images, yielding lock-in amplitude A and phase ϕ images, with the A images providing the magnitude of the AEE-induced temperature modulation and the ϕ images providing information on the sign of the temperature modulation and the time delay due to thermal diffusion.

Figures 1c and 1d, respectively, display the A and ϕ images for a Mn_3Sn slab with (2 $\bar{1}$ 10) oriented surface at

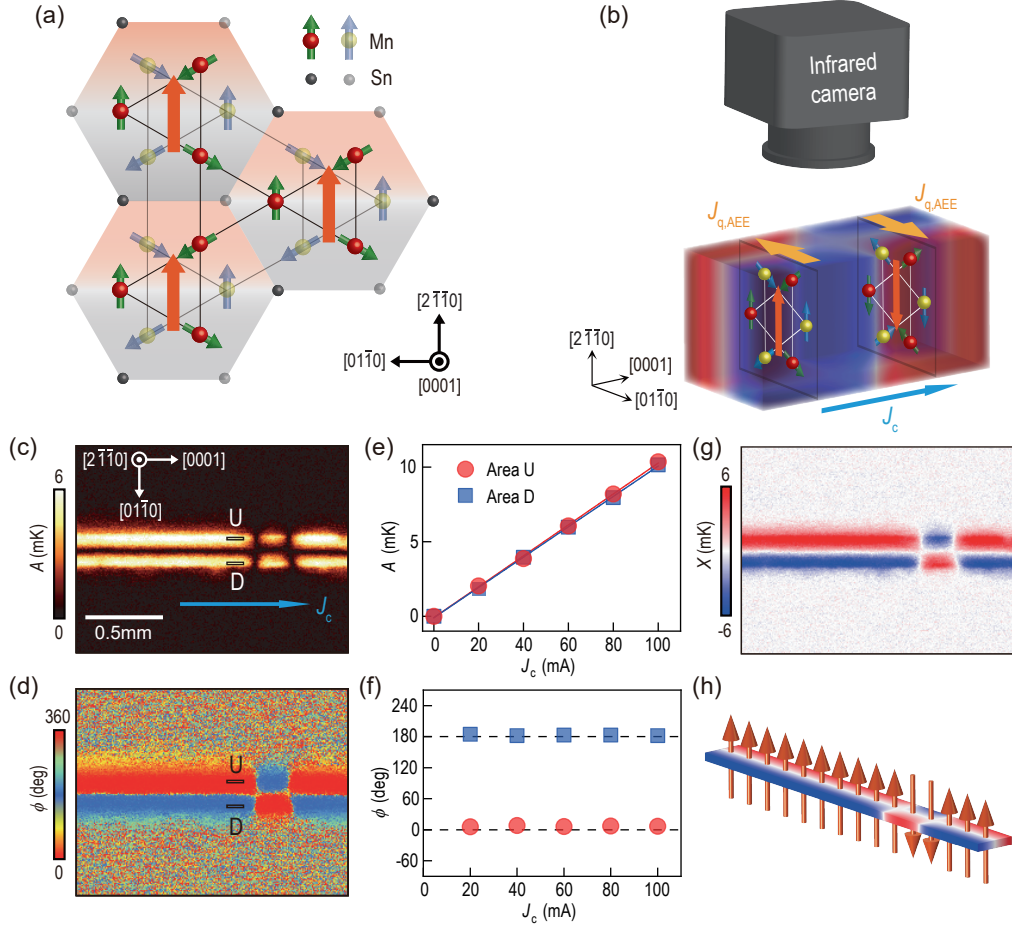


FIG. 1. Magnetic structure of Mn_3Sn and infrared imaging of magnetic domains by the AEE. **a**, Red and yellow spheres denote Mn atoms on two stacked kagome planes, and the arrows on the atoms represent the moments. The spin texture can be viewed as a ferroic order of a cluster magnetic octupole. The orange arrows represent the direction of the octupole moment. **b**, A schematic of infrared imaging of magnetic octupole domains with opposite polarization using the AEE. \mathbf{J}_c and $\mathbf{J}_{q,\text{AEE}}$ denote the applied charge current and heat current generated by the AEE, respectively. **c,d**, Lock-in amplitude A and phase ϕ images for the $(2\bar{1}\bar{1}0)$ plane of a Mn_3Sn slab with an out-of-plane easy axis at $J_c = 50$ mA along the $[0001]$ direction. **e,f**, J_c dependence of A and ϕ in the regions of interest on the Mn_3Sn slab which are defined by two rectangles marked with U and D. The plotted data was obtained by averaging the values in each area, which consists of 28 pixels. **g**, Image of $X = A\cos\phi$. **h**, Magnetic octupole domain patterns of the Mn_3Sn slab revealed by the temperature modulation in **g**.

zero magnetic field after oscillation demagnetization and $J_c = 50$ mA along the $[0001]$ direction. All Mn_3Sn crystal samples used in this study were grown by bismuth flux method without polishing, from which Kerr signal can not be detected probably due to surface oxidization and roughness (see Supplementary Fig. S1). We observe three clearly distinct temperature-modulation regions, where the left and right regions show temperature increase and decrease in the up and down halves while the middle region shows an opposite pattern, indicating opposite in-plane temperature gradients along $[01\bar{1}0]$. For quantitative analysis, two regions of interest along $[01\bar{1}0]$, denoted as U and D, are defined on the Mn_3Sn slab. In Figs. 1e and 1f, we show the J_c dependence of A and ϕ for U and D. The plotted data is obtained by averaging

the values in each area. The A values are proportional to J_c , while the ϕ values remain unchanged with respect to J_c and exhibit a 180-degree shift for the U and D regions, which is in good agreement with the features of the AEE with the local \mathbf{p} along the $[2\bar{1}\bar{1}0]$ direction.

Figure 1g shows the $X = A\cos\phi$ image calculated from 1c and 1d. The use of $X = A\cos\phi$ to represent temperature modulation with sign information is more intuitive and easier to calculate the orientation of octupole domains in the absence of a significant phase delay. Therefore, throughout the following text, we adopt the X image to present the spatial distribution of temperature modulation. Taking into account the magnetic anisotropy that tends to align \mathbf{p} along the $[2\bar{1}\bar{1}0]$ direction[44–46], these observations strongly suggest that

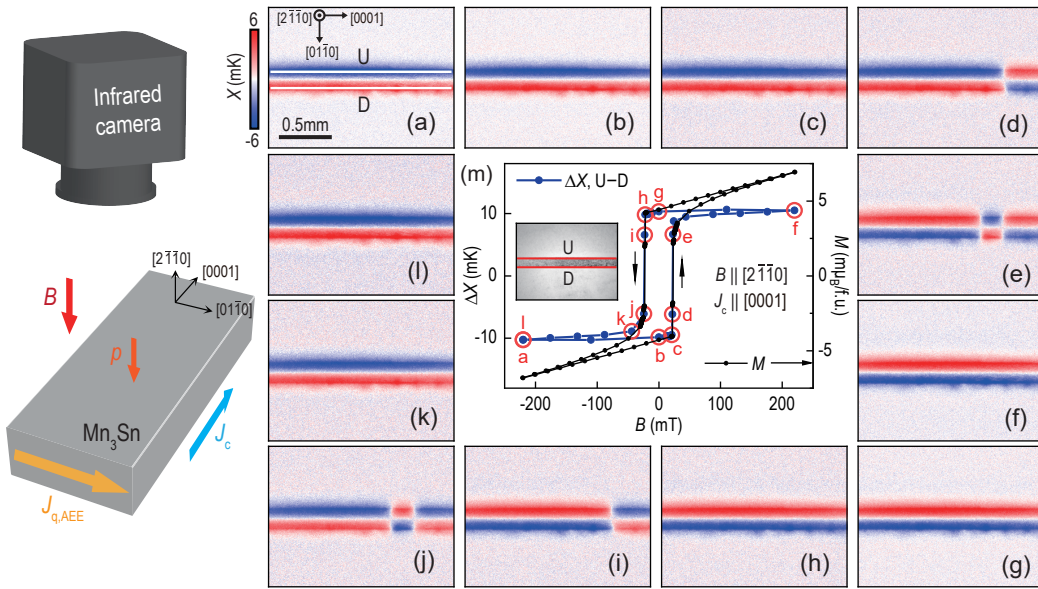


FIG. 2. Infrared imaging of magnetic domain patterns in Mn_3Sn during out-of-plane magnetic reversal. **a-l**, X images obtained in the out-of-plane field-scan cycle from -220 mT to 220 mT along $[2\bar{1}\bar{1}0]$ at $J_c = 50$ mA along $[0001]$. **m**, Field dependence of ΔX calculated from the U and D areas of the Mn_3Sn slab, where the plotted data were obtained by subtracting the average values on D from U, which consists of 640 pixels. For comparison, the field dependence of the magnetization M is shown. Inset shows the DC infrared image of the $(2\bar{1}\bar{1}0)$ surface plane of the Mn_3Sn slab. The thickness and width of the slab are approximately 0.09 mm and 0.17 mm, with a charge current density of $j_c = 3.3 \times 10^3$ A m^{-2} .

the sample has a domain distribution with upward oriented \mathbf{p} on the left and right sides and downward oriented \mathbf{p} in the middle. Assuming the AEE as the origin of the thermal patterns, we plot in Fig. 1h the magnetic octupole domain patterns of the Mn_3Sn slab that are revealed by the X image in Fig. 1g.

Imaging the out-of-plane magnetic reversal of Mn_3Sn

To verify the validity of the AEE for imaging octupole domain structures, we applied it to visualize the domain reversal by external magnetic fields. Figure 2a–2l display a series of X images of the same sample as in Fig. 1c under the out-of-plane field-scan cycle from -220 mT to 220 mT along $[2\bar{1}\bar{1}0]$. The applied current J_c is 50 mA in the $[0001]$ direction, which generates a temperature gradient in the $[01\bar{1}0]$ direction (Fig. 2a). To evaluate the temperature difference along this direction, we defined two regions of interest, labeled as U and D (Fig. 2a, and inset of Fig. 2m), which respectively cover the upper and lower edges of the Mn_3Sn slab. Fig. 2m plots the field dependence of ΔX , which is calculated by subtracting the average X values of D from those of U. The resulting ΔX curve exhibits a closed hysteresis loop, analogous to its AHE curve (see Supplementary Fig. S2a). For comparison, the field dependence of the magnetization M is plotted in Fig. 2m. Apart from a linear background,

ΔX curve is in good agreement with the M hysteresis loop (see Supplementary Fig. S3a for further comparison). The ΔX curve obtained using this technique is similar to the temperature gradient results observed from transport measurements[38]. However, the corresponding X images provide visualization of the domain evolution at each point (i.e., points a-l) of the curve, which is beyond the capacity of transport measurements. Based on the calculated thermal gradient ∇T along $[01\bar{1}0]$, the AEE coefficient of Mn_3Sn is estimated to be $|\varepsilon_{\text{AEE}}| \approx 18$ $\mu\text{K} \cdot \text{A}^{-1}$, which is the first experimentally determined value for this material. The ANE coefficient $|S_{\text{ANE}}|$ of Mn_3Sn reported by Li *et al.*[11] is about 0.5 $\mu\text{V} \text{K}^{-1}$ at room temperature, with a thermal conductivity κ of approximately 7.4 $\text{W} \text{K}^{-1}\text{m}^{-1}$. Using the Bridgman relation $\varepsilon_{\text{AEE}} = TS_{\text{ANE}}/\kappa$ [41], this predicts an AEE coefficient $|\varepsilon_{\text{AEE}}|$ of about 20 $\mu\text{K} \cdot \text{A}^{-1}$, which is close to our measured value.

Figures 2b and 2g show the domain patterns under zero external magnetic field, which are nearly identical to those observed in Figs. 2a and 2f under saturation fields, confirming a spontaneous AEE at zero field whose sign can be switched by a coercive field ~ 23 mT. Meanwhile, Figures 2d, 2e, 2i, and 2j reveal four intermediate states during the reversal process, showing three sizeable single-domain regions separated by two (0001) facets. These single-domain regions undergo a sharp reversal along the $[2\bar{1}\bar{1}0]$ easy axis even in a field scanning with field sweeps by a 0.01 mT step. It should be noted that although

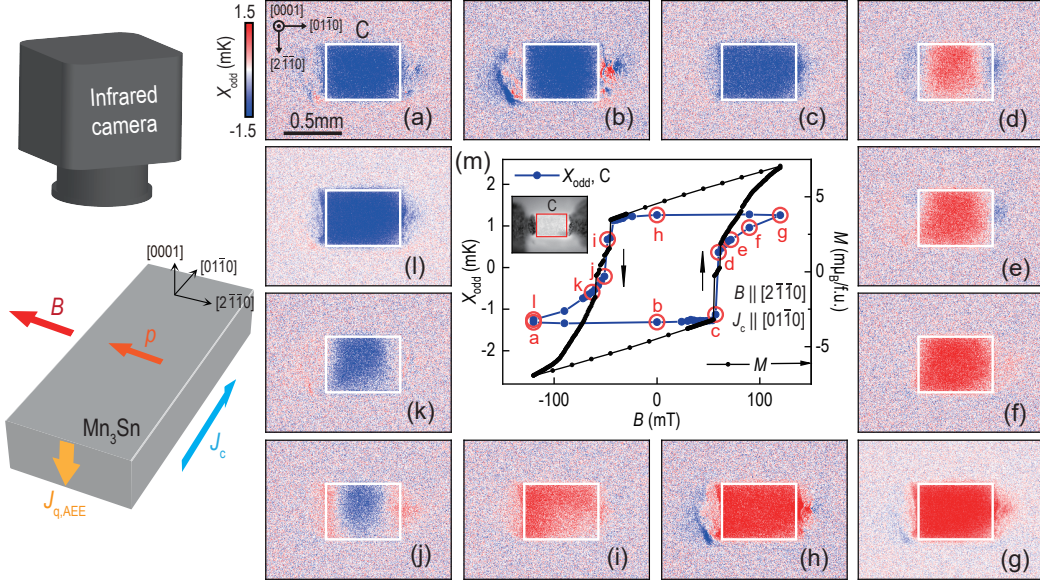


FIG. 3. Infrared imaging of magnetic domain patterns in Mn_3Sn during in-plane magnetic reversal. **a-l**, X_{odd} images obtained in the in-plane field-scan cycle from -120 mT to 120 mT along $[2\bar{1}\bar{1}0]$ at $J_c = 50$ mA along $[01\bar{1}0]$, where X_{odd} denotes the lock-in temperature modulation with the B -odd dependence. **m**, Field dependence of X_{odd} on the C area of the Mn_3Sn slab, where the plotted data was obtained by averaging the values on C, which consists of 10800 pixels. For comparison, the field dependence of the magnetization M is shown. Inset shows the DC infrared image of the Mn_3Sn slab with the surface along the (0001) direction. The thickness and width of the slab are approximately 0.12 mm and 0.45 mm, with a charge current density of $j_c = 0.9 \times 10^3$ A m^{-2} .

each domain region in this sample exhibits a sharp reversal along easy axis, the reversal behavior can vary significantly between samples (see Supplementary Fig. S4). Furthermore, the LIT imaging, as well as other imaging methods such as MOKE and ANE, can only visualize domain regions composed of a large number of magnetic octupoles and cannot resolve the spin structure of magnetic octupoles or the internal structure of domain walls.

Imaging the in-plane magnetic reversal of Mn_3Sn

Figure 3 presents the results of in-plane domain reversal of a Mn_3Sn sample with the surface oriented along the (0001) direction. Figure 3a-3l display the X_{odd} images obtained through an in-plane field-scan cycle ranging from -120 mT to 120 mT along $[2\bar{1}\bar{1}0]$ at $J_c = 50$ mA along $[01\bar{1}0]$. Here, $X_{\text{odd}} = A_{\text{odd}} \cos \phi_{\text{odd}}$ refers to the lock-in temperature modulation with B -odd dependence, which eliminates a background primarily originating from the Peltier effect of the two contact electrodes[32], where $A_{\text{odd}} e^{i\phi_{\text{odd}}} = [A e^{i\phi} - (A_{\text{maxB}} e^{i\phi_{\text{maxB}}} + A_{\text{minB}} e^{i\phi_{\text{minB}}})/2]$, and $A_{\text{maxB}} (\phi_{\text{maxB}})$ and $A_{\text{minB}} (\phi_{\text{minB}})$ represent the lock-in amplitude (phase) at the maximum positive magnetic field and minimum negative magnetic field, respectively. In this configuration, the temperature gradient of the AEE is in the out-of-plane direction, resulting in the formation of cor-

responding heating or cold cooling regions on the surface, depending on the direction of the in-plane octupole moment. Thus, the color change from blue to red and back to blue in Figs. 3a-3l corresponds to the in-plane reversal process along the $[2\bar{1}\bar{1}0]$ direction. Fig. 3m illustrates the field dependence of the averaged X_{odd} on the C region (defined in Fig. 3a, and inset of Fig. 3m), which exhibits a hysteresis loop. For comparison, the field dependence of the magnetization M is also shown in Fig. 3m, and they are in a good agreement (Supplementary Fig. S3b). By combining the X_{odd} images at selected points on the hysteresis (e.g., Figs. 3d, 3e, 3j, and 3k), it is suggested that the in-plane reversal of this sample involves a rather gradual process of \mathbf{p} rotation initially in the middle and then on both sides. The results in Fig. 2 and 3 demonstrate the effectiveness of the AEE as a versatile tool to observe both out-of-plane and in-plane octupole domain structures.

Imaging the in-plane and out-of-plane magnetic reversals of Mn_3Ge

Figure 4 presents the results of out-of-plane and in-plane domain reversals of a Mn_3Ge sample with the surface oriented along the $[2\bar{1}\bar{1}0]$ direction. Figure 4a-4l display the X_{odd} images obtained through an out-of-plane field-scan cycle ranging from -220 mT to 220 mT along

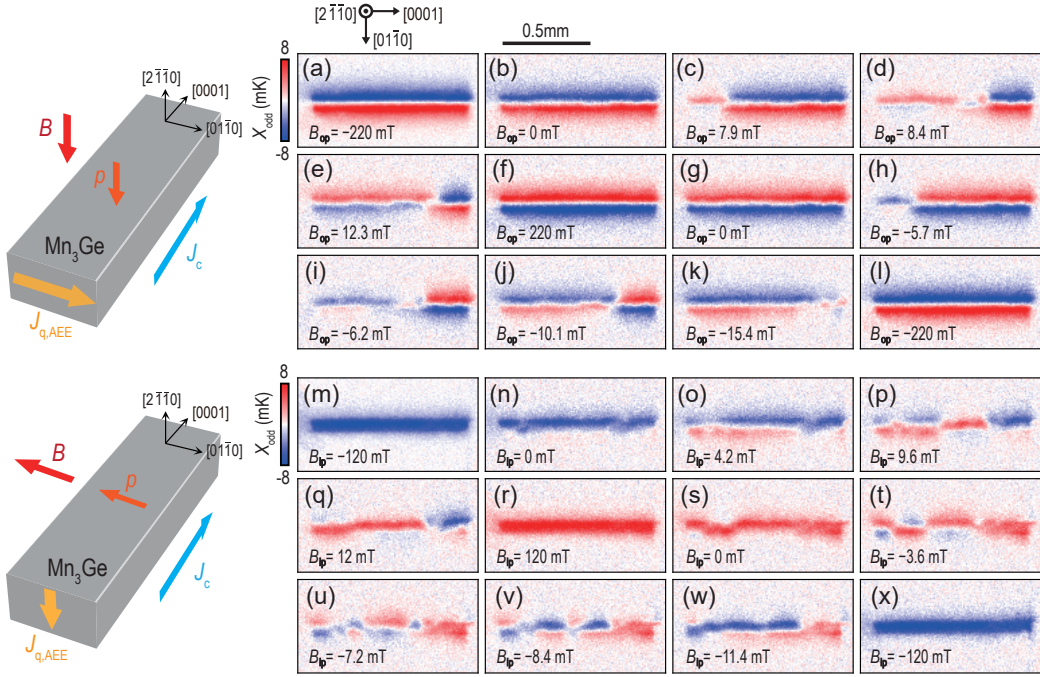


FIG. 4. Infrared imaging of magnetic domain patterns in Mn_3Ge during out-of-plane and in-plane magnetic reversals. **a-l**, X_{odd} images obtained in the out-of-plane field-scan cycle from -220 mT to 220 mT along $[2\bar{1}\bar{1}0]$ at $J_c = 50$ mA along $[0001]$. **m-x**, X_{odd} images obtained in the in-plane field-scan cycle from -120 mT to 120 mT along $[01\bar{1}0]$ at $J_c = 50$ mA along $[0001]$. X_{odd} denotes the lock-in temperature modulation with the B -odd dependence.

$[2\bar{1}\bar{1}0]$ at $J_c = 50$ mA along $[0001]$. Analysis of Fig. 4c-4e and Fig. 4h-4j indicates that the out-of-plane domain reversal process in this sample proceeds from left to right, rather than being a sharp transition directly from up to down, passing through the $[01\bar{1}0]$ direction. Figure 4m-4x display the X_{odd} images obtained through an in-plane field-scan cycle ranging from -120 mT to 120 mT along $[01\bar{1}0]$ at $J_c = 50$ mA along $[0001]$. It is evident that the in-plane reversal process also occurs from left to right and involves traversing the $[2\bar{1}\bar{1}0]$ direction. The results presented in Fig. 4 exemplify the versatility of our infrared imaging technique in studying the Mn_3X family. The ANE coefficient $|S_{\text{ANE}}|$ of Mn_3Ge reported by Tomita *et al.*[47] is about $0.35 \mu\text{V K}^{-1}$ at 300 K, with a thermal conductivity κ of approximately $6.6 \text{ W K}^{-1}\text{m}^{-1}$. The AEE coefficient $|\varepsilon_{\text{AEE}}|$ of Mn_3Ge was first measured by Xu *et al.*[38], which is about $15 \mu\text{K m}\cdot\text{A}^{-1}$ at 300 K. The value we estimated by LIT is about $17 \mu\text{K m}\cdot\text{A}^{-1}$, close to their value by transport measurements.

Visualization of the magnetic memory effect

Figure 5 presents the visualization for the prior-field-dependent chirality of octupole rotation during in-plane magnetic field sweep, which is due to the “memory effect” in Mn_3Sn [13]. Fig. 5a illustrates the initial out-of-plane orientation of \mathbf{p} in a Mn_3Sn slab after applying a

prior field of -60 mT along $[2\bar{1}\bar{1}0]$, which is evidenced by the in-plane temperature gradient in the measured X_{odd} image obtained at $J_c = 50$ mA along $[0001]$. Fig. 5b-5f illustrates the out-of-plane rotation of \mathbf{p} during an in-plane field-scan cycle, along with the corresponding X_{odd} images. In Fig. 5b, 5d and 5f, uniform temperature distributions similar to that in Fig. 3a are found, indicating \mathbf{p} alignment parallel to the in-plane field. In Fig 5c and 5e, in-plane temperature gradient similar to that in Fig. 5a is found, which means that the initial out-of-plane orientation of \mathbf{p} can be recovered at a low field during the in-plane field sweeping. Therefore, \mathbf{p} shows an anti-clockwise rotation from $B_{\text{ip}} = -240$ mT to $B_{\text{ip}} = 240$ mT and a clockwise rotation from $B_{\text{ip}} = 240$ mT to $B_{\text{ip}} = -240$ mT. Fig. 5g-5l shows the measured X_{odd} images for the in-plane field sweep after a reversed prior field, $B_{\text{op}} = 60$ mT. The thermal images show that \mathbf{p} is aligned parallelly with the in-plane field at $B_{\text{ip}} = \pm 240$ mT but has an opposite out-of-plane orientation in the low field range compared to those in Fig. 5c-5e, evidencing the prior-field-dependent rotation chirality of \mathbf{p} . In previous studies, the prior-field-dependent rotation chirality of \mathbf{p} in the “memory effect” was proposed to understand the planar AHE and planar ANE during an in-plane magnetic field sweeping[13, 48], which was not directly observed. Here the LIT measurement clarifies the microscopic origin of the “memory effect” in Mn_3Sn . Compared to MOKE which allows observation of the \mathbf{p}

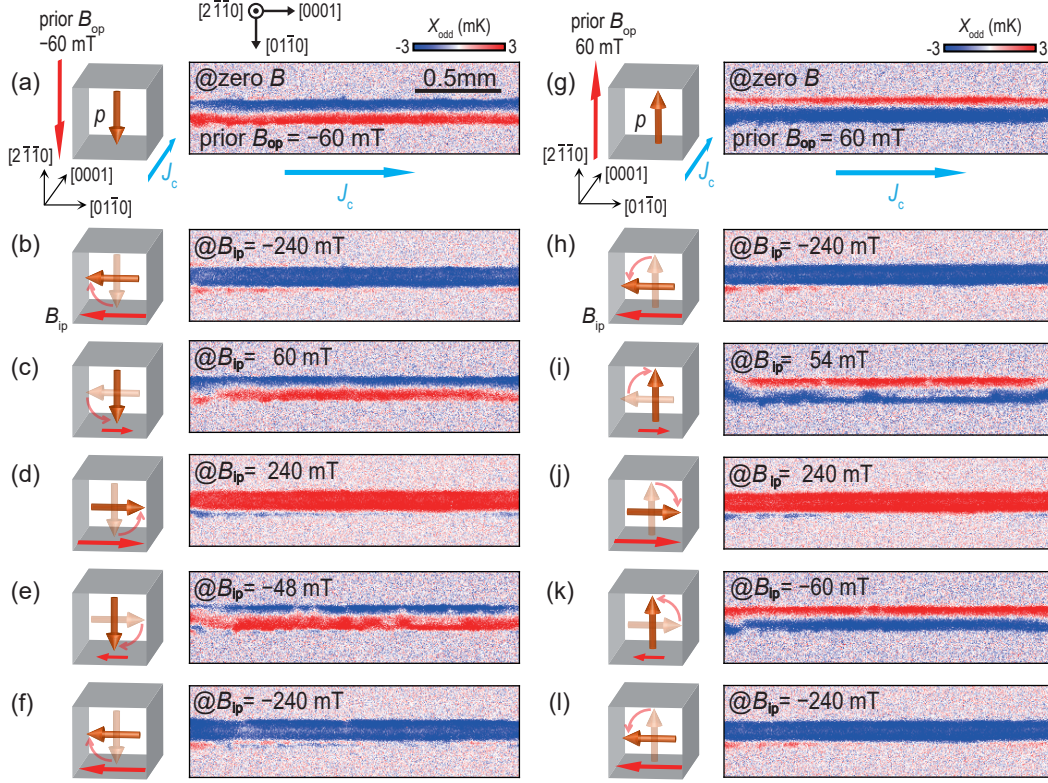


FIG. 5. Visualization of the magnetic memory effect by the anomalous Ettingshausen effect in Mn_3Sn . **a,g**, The initial orientation of the octupole moment and the corresponding X_{odd} image obtained at zero field and $J_c = 50$ mA along $[0001]$, after applying a prior field $B_{\text{op}} = -60$ mT (**a**) and $B_{\text{op}} = 60$ mT (**g**) along $[2\bar{1}\bar{1}0]$. **b-f,h-l**, The out-of-plane rotation of the octupole moment during an in-plane field-scan cycle from -240 mT to 240 mT along $[01\bar{1}0]$, and the corresponding measured X_{odd} images, with the prior field $B_{\text{op}} = -60$ mT (**b-f**) and $B_{\text{op}} = 60$ mT (**h-l**). The chirality of the octupole moment rotation is found to depend on the direction of the prior field.

component along one direction in an optical setup[14, 16], our method offers a clear benefit for investigating 3D octupole moments dynamic processes.

METHODS

Preparation of Mn_3Sn samples

CONCLUSIONS

In summary, we have developed a new technique for visualizing the octupole domain structure in non-collinear AFMs using the AEE at room temperature. The AEE imaging of the domain configurations in non-collinear AFMs may well accelerate the development of future memory devices and facilitate the study of current-driven domain dynamics. Our preliminary *ab initio* calculation shows the AEE is sizable in several materials in the Mn_3X family, indicating its wide application. Furthermore, some non-collinear antiferromagnetic materials may exhibit a small Kerr angle but a large AEE coefficient, for which this technique is particularly advantageous.

The Mn_3Sn single crystals were grown by the flux method using Bi as the flux. Mn powder (99.95% purity), Sn granules (99.999% purity), and Bi granules (99.999% purity) were mixed in a 3:1:3 molar ratio. This mixture was loaded into an alumina crucible, sealed in a quartz ampoule under a partial argon atmosphere, and heated to 1150 °C in a furnace within 15 hours, maintaining this temperature for 10 hours. The assembly was then slowly cooled to 700 °C at a rate of 50 °C per hour, held at that temperature for 10 hours, and further gradually cooled to 300 °C at a rate of 2 °C per hour, maintaining it for 50 hours. Finally, the assembly was taken out from the furnace, and Mn_3Sn crystals were separated from the flux using a centrifuge.

Sample characterization

The LIT measurement was made by the Luxet thermo 100 system produced by Suzhou Luxet Infrared Technology Co., Ltd. The magnetization was measured using a commercial superconducting quantum interference device magnetometer (MPMS, Quantum Design). The Hall resistivity was measured using a standard four-probe geometry with a 10 mA current. Magneto-optical imaging of Mn₃Sn crystals with (2 $\bar{1}$ 10) oriented surface plane was performed at room temperature using a Kerr microscope with 620 nm wavelength LED (TuoTuo Technology).

Experimental setup

The LIT system is composed of an infrared camera, a microscope lens, a system processing unit that performs real-time Fourier analysis of detected thermal images, and a source meter. Electromagnets situated underneath the infrared camera enable the measurement of thermal images under in-plane or out-of-plane magnetic fields. To prevent vibrations from interfering with the measurements, the camera and electromagnet are situated on a vibration isolation table. All Mn₃Sn samples used in this study were unpolished and their surfaces were coated with insulating black ink for LIT measurements.

ACKNOWLEDGEMENTS

The authors thank Z.G. Liang and L.F. Wang for the magnetization measurement. The study was supported by the supercomputing service of USTC, and the USTC Center for Micro- and Nanoscale Research and Fabrication.

FUNDING

This work was supported by the National Key R&D Program (2022YFA1403502), the National Natural Science Foundation of China (12234017,12074366), the Fundamental Research Funds for the Central Universities (WK9990000116). Y.F.G. acknowledges the support from the Shanghai Science and Technology Innovation Action Plan (21JC1402000) and the Double First-Class Initiative Fund of ShanghaiTech University. Y. Gao is supported by the Fundamental Research Funds for the Central Universities (WK2340000102). Z. Liu is supported by the National Natural Science Foundation of China (11974327 and 12004369), Fundamental Research Funds for the Central Universities (WK3510000010, WK2030020032), Anhui Initiative in Quantum Information Technologies (AHY170000), and

Innovation Program for Quantum Science and Technology (2021ZD0302800).

AUTHOR CONTRIBUTIONS

D.H., Y.F.G., P.W., and W.X. designed the experiment, W.X., Z.X., P.W., and J.S. fabricated the samples and collected all of the data. Y.C., W.P., J.Z., H.P., X.Y. and H.Y. contributed to the experimental set-up. P.W., D.H., and Y.F.G. analyzed the data. Q.N., Y.G. and Z.L. contribute theoretical discussions. D.H. and Y.F.G. supervised this study. All the authors discussed the results and prepared the manuscript.

Conflict of interest statement. None declared.

-
- [1] Higo T, Kondou K, Nomoto T *et al.* Perpendicular full switching of chiral antiferromagnetic order by current. *Nature* 2022; **607**: 474–479.
 - [2] Tsai H, Higo T, Kondou K *et al.* Electrical manipulation of a topological antiferromagnetic state. *Nature* 2020; **580**: 608–613.
 - [3] Liu ZQ, Chen H, Wang JM *et al.* Electrical switching of the topological anomalous Hall effect in a non-collinear antiferromagnet above room temperature. *Nat Electron* 2018; **1**: 172–177.
 - [4] Qin P, Yan H, Wang X *et al.* Room-temperature magnetoresistance in an all-antiferromagnetic tunnel junction. *Nature* 2023; **613**: 485–489.
 - [5] Chen X, Higo T, Tanaka K *et al.* Octupole-driven magnetoresistance in an antiferromagnetic tunnel junction. *Nature* 2023; **613**: 490–495.
 - [6] Jeon KR, Hazra BK, Kim JK *et al.* Chiral antiferromagnetic josephson junctions as spin-triplet supercurrent spin valves and d.c. SQUIDS. *Nat Nanotechnol* 2023; **18**: 747–753.
 - [7] Deng Y, Liu X, Chen Y *et al.* All-electrical switching of a topological non-collinear antiferromagnet at room temperature. *Natl Sci Rev* 2022; **10**: nwac154.
 - [8] Hu S, Shao DF, Yang H *et al.* Efficient perpendicular magnetization switching by a magnetic spin Hall effect in a noncollinear antiferromagnet. *Nat Commun* 2022; **13**: 4447.
 - [9] Nakatsuji S, Kiyohara N and Higo T. Large anomalous Hall effect in a non-collinear antiferromagnet at room temperature. *Nature* 2015; **527**: 212–215.
 - [10] Ikhlas M, Tomita T, Koretsune T *et al.* Large anomalous Nernst effect at room temperature in a chiral antiferromagnet. *Nat Phys* 2017; **13**: 1085–1090.
 - [11] Li X, Xu L, Ding L *et al.* Anomalous Nernst and Righi-Leduc Effects in Mn₃Sn: Berry Curvature and Entropy Flow. *Phys Rev Lett* 2017; **119**: 056601.
 - [12] Kuroda K, Tomita T, Suzuki MT *et al.* Evidence for magnetic Weyl fermions in a correlated metal. *Nat Mater* 2017; **16**: 1090–1095.
 - [13] Li X, Collignon C, Xu L *et al.* Chiral domain walls of Mn₃Sn and their memory. *Nat Commun* 2019; **10**: 3021.

- [14] Higo T, Man H, Gopman DB *et al.* Large magneto-optical Kerr effect and imaging of magnetic octupole domains in an antiferromagnetic metal. *Nat Photonics* 2018; **12**: 73–78.
- [15] Reichlova H, Janda T, Godinho J *et al.* Imaging and writing magnetic domains in the non-collinear antiferromagnet Mn_3Sn . *Nat Commun* 2019; **10**: 5459.
- [16] Uchimura T, Yoon JY, Sato Y *et al.* Observation of domain structure in non-collinear antiferromagnetic Mn_3Sn thin films by magneto-optical Kerr effect. *Appl Phys Lett* 2022; **120**: 172405.
- [17] Yan GQ, Li S, Lu H *et al.* Quantum Sensing and Imaging of Spin–Orbit-Torque-Driven Spin Dynamics in the Non-Collinear Antiferromagnet Mn_3Sn . *Adv Mater* 2022; **34**: 2200327.
- [18] Stöhr J, Scholl A, Regan TJ *et al.* Images of the Antiferromagnetic Structure of a NiO(100) Surface by Means of X-Ray Magnetic Linear Dichroism Spectromicroscopy. *Phys Rev Lett* 1999; **83**: 1862–1865.
- [19] Scholl A, Stöhr J, Lüning J *et al.* Observation of Antiferromagnetic Domains in Epitaxial Thin Films. *Science* 2000; **287**: 1014–1016.
- [20] Hedrich N, Wagner K, Pylypovskiy OV *et al.* Nanoscale mechanics of antiferromagnetic domain walls. *Nat Phys* 2021; **17**: 574–577.
- [21] Krizek F, Reimers S, Kašpar Z *et al.* Atomically sharp domain walls in an antiferromagnet. *Sci Adv* 2022; **8**: eabn3535.
- [22] Xu J, Zhou C, Jia M *et al.* Imaging antiferromagnetic domains in nickel oxide thin films by optical birefringence effect. *Phys Rev B* 2019; **100**: 134413.
- [23] Takeuchi Y, Yamane Y, Yoon JY *et al.* Chiral-spin rotation of non-collinear antiferromagnet by spin-orbit torque. *Nat Mater* 2021; **20**: 1364–1370.
- [24] Safeer CK, Juárez E, Lopez A *et al.* Spin–orbit torque magnetization switching controlled by geometry. *Nat Nanotechnol* 2015; **11**: 143–146.
- [25] Tang M, Shen K, Xu S *et al.* Bulk Spin Torque-Driven Perpendicular Magnetization Switching in $L1_0$ FePt Single Layer. *Adv Mater* 2020; **32**: 2002607.
- [26] Liu L, Zhou C, Shu X *et al.* Symmetry-dependent field-free switching of perpendicular magnetization. *Nat Nanotechnol* 2021; **16**: 277–282.
- [27] Wang Y, Taniguchi T, Lin PH *et al.* Time-resolved detection of spin–orbit torque switching of magnetization and exchange bias. *Nat Electron* 2022; **5**: 840–848.
- [28] Xu J, Xia J, Zhang X *et al.* Exchange-Torque-Triggered Fast Switching of Antiferromagnetic Domains. *Phys Rev Lett* 2022; **128**: 137201.
- [29] Wu M, Isshiki H, Chen T *et al.* Magneto-optical Kerr effect in a non-collinear antiferromagnet Mn_3Ge . *Appl Phys Lett* 2020; **116**: 132408.
- [30] Ken-ichi Uchida and Shunsuke Daimon and Ryo Iguchi and Eiji Saitoh. Observation of anisotropic magneto-Peltier effect in nickel. *Nature* 2018; **558**: 95–99.
- [31] Wang J, Takahashi YK and ichi Uchida K. Magneto-optical painting of heat current. *Nat Commun* 2020; **11**: 2.
- [32] Breitenstein O, Warta W and Langenkamp M. *Lock-in thermography: Basics and use for evaluating electronic devices and materials*, (Springer2010), 2nd edition.
- [33] Seki T, Iguchi R, Takanashi K *et al.* Visualization of anomalous Ettingshausen effect in a ferromagnetic film: Direct evidence of different symmetry from spin Peltier effect. *Appl Phys Lett* 2018; **112**: 152403.
- [34] Daimon S, Iguchi R, Hioki T *et al.* Thermal imaging of spin Peltier effect. *Nat Commun* 2016; **7**: 13754.
- [35] Suzuki MT, Koretsune T, Ochi M *et al.* Cluster multipole theory for anomalous Hall effect in antiferromagnets. *Phys Rev B* 2017; **95**: 094406.
- [36] Chen H, Niu Q and MacDonald A. Anomalous Hall Effect Arising from Noncollinear Antiferromagnetism. *Phys Rev Lett* 2014; **112**: 017205.
- [37] Yang H, Sun Y, Zhang Y *et al.* Topological Weyl semimetals in the chiral antiferromagnetic materials Mn_3Ge and Mn_3Sn . *New J Phys* 2017; **19**: 015008.
- [38] Xu L, Li X, Lu X *et al.* Finite-temperature violation of the anomalous transverse Wiedemann-Franz law. *Sci Adv* 2020; **6**: eaaz3522.
- [39] Chen T, Tomita T, Minami S *et al.* Anomalous transport due to Weyl fermions in the chiral antiferromagnets Mn_3X , X = Sn, Ge. *Nat Commun* 2021; **12**: 572.
- [40] Nagamiya T, Tomiyoshi S and Yamaguchi Y. Triangular spin configuration and weak ferromagnetism of Mn_3Sn and Mn_3Ge . *Solid State Commun* 1982; **42**: 385–388.
- [41] Bridgman PW. The Connections between the Four Transverse Galvanomagnetic and Thermomagnetic Phenomena. *Phys Rev* 1924; **24**: 644–651.
- [42] Miura A, Sepehri-Amin H, Masuda K *et al.* Observation of anomalous Ettingshausen effect and large transverse thermoelectric conductivity in permanent magnets. *Appl Phys Lett* 2019; **115**: 222403.
- [43] Seki T, Miura A, ichi Uchida K *et al.* Anomalous Ettingshausen effect in ferrimagnetic Co–Gd. *Appl Phys Express* 2019; **12**: 023006.
- [44] Duan TF, Ren WJ, Liu WL *et al.* Magnetic anisotropy of single-crystalline Mn_3Sn in triangular and helix-phase states. *Appl Phys Lett* 2015; **107**: 082403.
- [45] Li X, Zhu Z and Behnia K. A Monomaterial Nernst Thermopile with Hermaphroditic Legs. *Adv Mater* 2021; **33**: 2100751.
- [46] Li X, Xu L, Zuo H *et al.* Momentum-space and real-space Berry curvatures in Mn_3Sn . *SciPost Phys* 2018; **5**: 063.
- [47] Tomita T, Minami S, Ikhlas M *et al.* Anomalous transport properties of the antiferromagnetic Weyl semimetals Mn_3X (X = Sn, Ge). *J Phys Conf Ser* 2022; **2164**: 012065.
- [48] Xu L, Li X, Ding L *et al.* Planar Hall effect caused by the memory of antiferromagnetic domain walls in Mn_3Ge . *Appl Phys Lett* 2020; **117**: 222403.

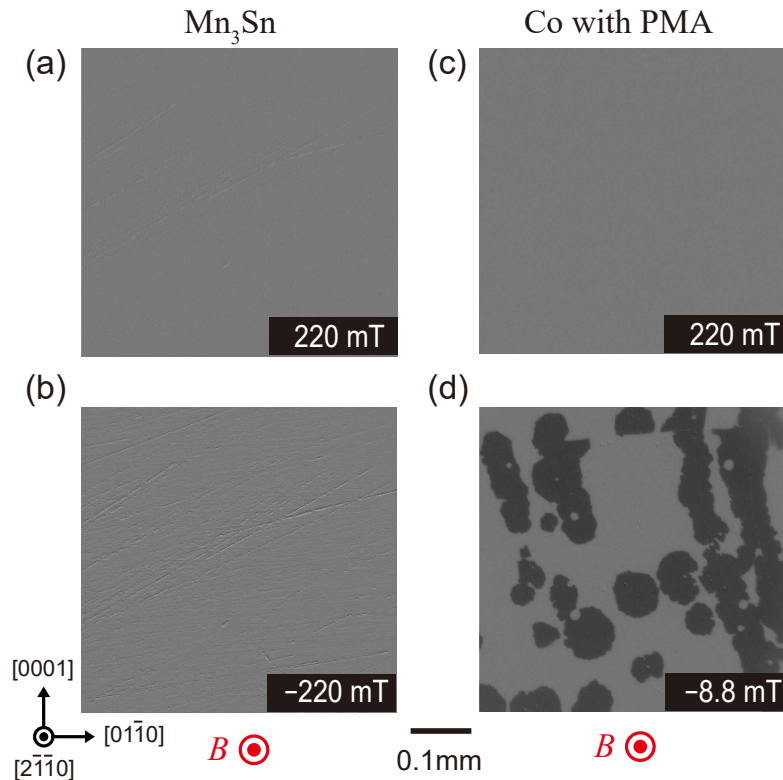
Supplementary Information for “Infrared Imaging of Magnetic Octupole Domains in Non-collinear Antiferromagnets”

CONTENTS

A. MOKE images of Mn_3Sn	1
B. The AHE and the optical image of the Mn_3Sn sample in Fig. 2	2
C. Compare the X curves to magnetization M	2
D. The out-of-plane AEE results of the same Mn_3Sn sample in Fig. 4	2
E. Movie of the out-of-plane magnetic reversal process in Mn_3Sn	2
F. The definition of the anomalous Ettingshausen coefficient	3
References	3

A. MOKE images of Mn_3Sn

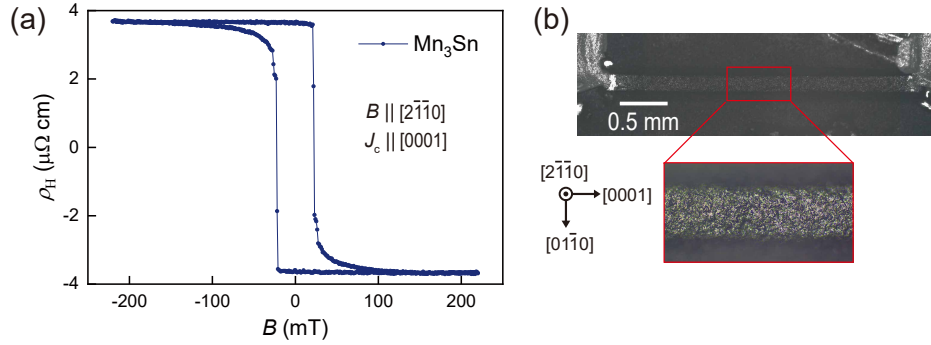
Figure S1 shows the MOKE images of Mn_3Sn . Kerr signal can not be detected probably due to surface oxidization and roughness. MOKE images of a 0.7-nm-thick Co film with perpendicular magnetic anisotropy (PMA) under the same set-up is also shown for comparison.



Supplementary Fig. S1. MOKE images of Mn_3Sn . **a,b**, MOKE images of Mn_3Sn obtained at an out-of-plane field $B = 220$ mT (**a**) and $B = -220$ mT (**b**). **c,d**, Moke images of a 0.7-nm-thick Co film with perpendicular magnetic anisotropy (PMA) for comparison obtained at $B = 220$ mT (**c**) and $B = -8.8$ mT (**d**). Grey and black regions correspond to positive and negative values of the MOKE signal.

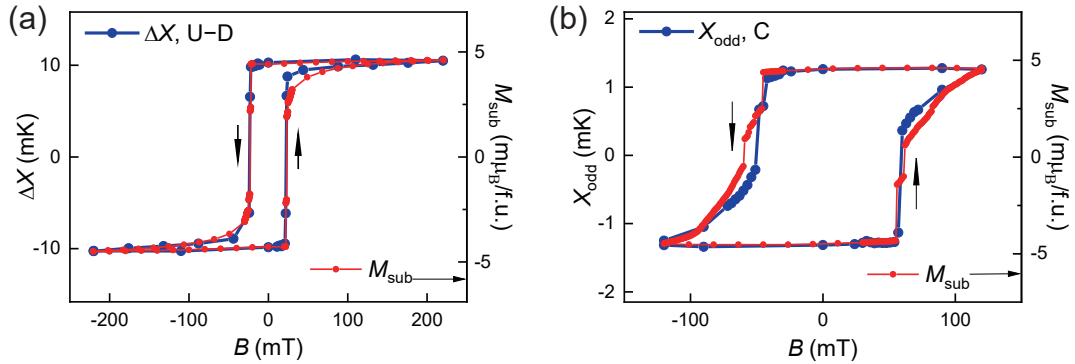
B. The AHE and the optical image of the Mn₃Sn sample in Fig. 2

Figure S2(a) shows the measured anomalous Hall effect (AHE) signal of the same Mn₃Sn sample in Fig. 1 and Fig. 2 in the main text. Figure S2(b) shows the optical image of this sample, which is covered with insulating black ink for lock-in thermography measurements.



Supplementary Fig. S2. The AHE (a) and the optical image (b) of the Mn₃Sn sample in Fig. 2.

C. Compare the X curves to magnetization M



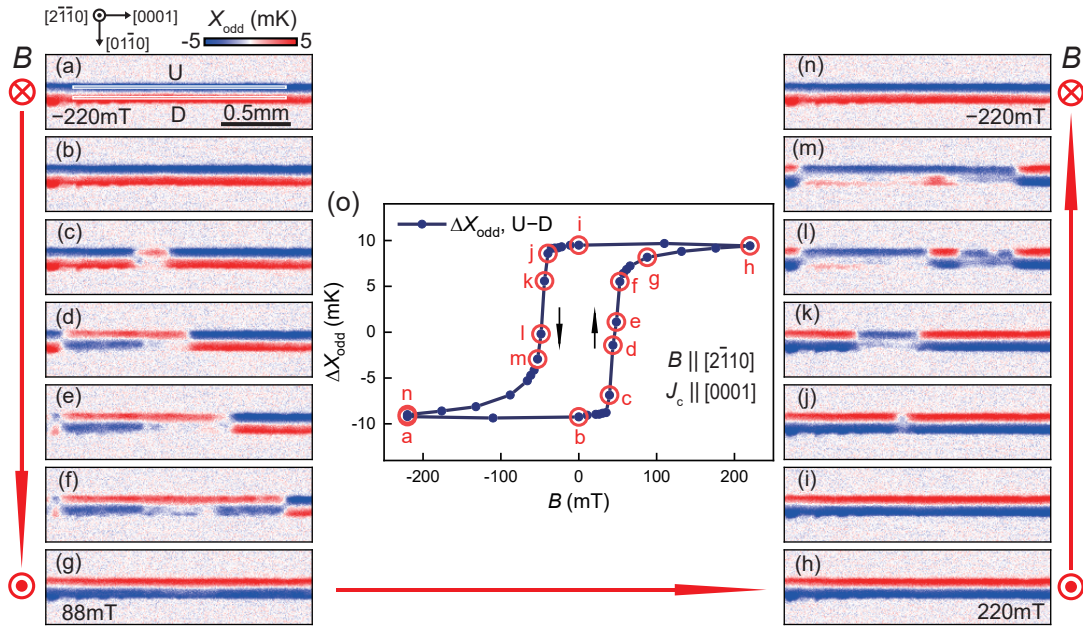
Supplementary Fig. S3. Compare the ΔX (or X_{odd}) curves in Fig. 2 and Fig. 3 to magnetization M subtracted by a linear function.

D. The out-of-plane AEE results of the same Mn₃Sn sample in Fig. 4

Figure S4 shows the X_{odd} images and the corresponding ΔX_{odd} curve obtained in the out-of-plane field-scan cycle of the same Mn₃Sn sample in Fig. 4 in the main text.

E. Movie of the out-of-plane magnetic reversal process in Mn₃Sn

Supplementary Movie S1. The movie of the out-of-plane magnetic reversal process under a more precise magnetic field scanning with a step of 0.01 mT for the same Mn₃Sn sample in Fig. 2 in the main text.



Supplementary Fig. S4. The out-of-plane AEE results of the same Mn_3Sn sample in Fig. 4. **a-n**, X_{odd} images obtained in the out-of-plane field-scan cycle from -220 mT to 220 mT along $[2\bar{1}10]$ at $J_c = 50$ mA along $[0001]$, where X_{odd} denotes the lock-in temperature modulation with the B -odd dependence. **o**, Field dependence of ΔX_{odd} calculated from the U and D areas of the Mn_3Sn slab, where the plotted data were obtained by subtracting the average values on D from U.

F. The definition of the anomalous Ettingshausen coefficient

There are two prevalent definitions for the anomalous Ettingshausen effect (AEE) coefficient in published literatures. The first defines the AEE coefficient as $\varepsilon_{\text{AEE}} = \nabla_y T / j_x$ [1, 2], where $\nabla_y T$ is the transverse thermal gradient generated by the AEE, and j_x is the longitudinal current density. This definition is equivalent to the one used in our study, $\nabla T_{\text{AEE}} = \varepsilon_{\text{AEE}}(\mathbf{j}_c \times \mathbf{p})$. Under this definition, the Bridgman relation, linking the AEE coefficient ε_{AEE} and the anomalous Nernst effect (ANE) coefficient S_{ANE} , is expressed as $\varepsilon_{\text{AEE}} = S_{\text{ANE}} T / \kappa$ [3, 4], with T being the absolute temperature and κ being the thermal conductivity.

The second definition characterizes the AEE coefficient as $\mathbf{j}_{\text{q,AEE}} = \Pi_{\text{AEE}}(\mathbf{j}_c \times \mathbf{m})$ [5, 6], where $\mathbf{j}_{\text{q,AEE}}$, Π_{AEE} , \mathbf{j}_c , and \mathbf{m} denote the heat current density generated by the AEE, the AEE coefficient, the charge current density, and the unit vector of magnetization \mathbf{M} , respectively. Under this definition, the Bridgman relation is $\Pi_{\text{AEE}} = S_{\text{ANE}} T$, which exhibits a formal similarity to the Kelvin relation $\Pi = ST$, with Π being the Peltier coefficient and S being the Seebeck coefficient.

Both definitions of the AEE coefficient are commonly employed, differing only in terms of the thermal conductivity κ . Since we did not directly measure thermal conductivity, we have adopted the first definition in our work.

-
- [1] Behnia K. *Fundamentals of Thermoelectricity*, Oxford University Press, 2015.
 - [2] Xu L, Li X, Lu X *et al.* Finite-temperature violation of the anomalous transverse Wiedemann-Franz law. *Sci Adv* 2020; **6**: eaaz3522.
 - [3] Bridgman PW. The Connections between the Four Transverse Galvanomagnetic and Thermomagnetic Phenomena. *Phys Rev* 1924; **24**: 644–51.
 - [4] Callen HB. The Application of Onsager's Reciprocal Relations to Thermoelectric, Thermomagnetic, and Galvanomagnetic Effects. *Phys Rev* 1948; **73**: 1349–58.
 - [5] Seki T, Iguchi R, Takanashi K *et al.* Relationship between anomalous Ettingshausen effect and anomalous Nernst effect in an FePt thin film. *J Phys D Appl Phys* 2018; **51**: 254001.
 - [6] Miura A, Sepehri-Amin H, Masuda K *et al.* Observation of anomalous Ettingshausen effect and large transverse thermoelectric conductivity in permanent magnets. *Appl Phys Lett* 2019; **115**: 222403.